Optimisation of hybrid composite shields for hypervelocity Micro-Meteoroid and Orbital Debris (MMOD) impact

Citation for published version:
Fowler, K & Teixeira-Dias, F 2024, 'Optimisation of hybrid composite shields for hypervelocity Micro-Meteoroid and Orbital Debris (MMOD) impact', *Advances in Space Research*, vol. 73, no. 12, pp. 6194-6208. https://doi.org/10.1016/j.asr.2024.03.071

Digital Object Identifier (DOI):
10.1016/j.asr.2024.03.071

Published In:
Advances in Space Research

Optimisation of hybrid composite shields for hypervelocity Micro-Meteoroid and Orbital Debris (MMOD) impact

K. Fowler[a], F. Teixeira-Dias[a,*]

[a] *Institute for Infrastructure and Environment (IIE)*
School of Engineering, The University of Edinburgh
Edinburgh EH9 3FG, United Kingdom

Abstract

Advancements in space exploration over the last few decades have led to a sharp increase in Micro-Meteoroid and Orbital Debris (MMOD), with the associated increased risk of hypervelocity impact on satellites and space structures. The Whipple shield can mitigate the effects of such impacts and current research is exploring further developments towards effective lightweight passive shielding technology to counter the damaging effects of MMOD. With the increase in MMOD and the prospect of increased space travel in the coming years and decades, it is vital that more research is conducted and improvements are made in the development and design of efficient, lightweight shielding technology to protect both unmanned and manned spacecraft against hypervelocity impacts (HVI). The optimisation of shield design for HVI is a high dimensionality problem, suited to advanced computational approaches. Key variables in HVI shield design that should inform the focus on optimisation include: impact velocity, rear wall thickness, projectile diameter and bumper thickness. A hybrid shield configuration and numerical model are proposed and validated, with alternating layers of aluminium (AL2024) and carbon fibre composites (CFRP, T300 woven-fabric) to form a 5 mm thick target plate consisting of 5 plies. The adaptive coupled FEM-SPH method is used to model the target plates. The proposed hypervelocity shield design optimisation methodology is based on Direct Simulation-based Genetic Algorithm (DSGA) optimisation and is implemented to optimise a multi-variable shield design space. Objective weightings are used to analyse and discuss results, referring to the ratio of the kinetic energy to the shield areal density objectives. A clear transition in the impact behaviour of the optimised MMOD shields is observed in the transition region from high-velocity to hypervelocity impact, where significant levels of kinetic energy dissipation are observed below the transition region, and lower energy dissipation at hypervelocity. The shield design optimisation results show that with a weighted kinetic energy to mass objective of 90:10, the kinetic energy of the back shield plate decreases significantly (62.7%) and the areal density can be reduced by more than 18%. Alternative configurations displayed sub-optimal results based on a trade-off between objective functions.

Keywords: Hypervelocity impact, Whipple shield, Space debris, Design optimisation, Direct Simulation-based Genetic Algorithm (DSGA), Adaptive coupled FEM-SPH

1. Background and introduction

Advancements in space exploration over the last few decades have led to a significant increase in Micro-Meteoroid and Orbital Debris (MMOD). The majority of this debris is a result of spacecraft break-ups, collisions and explosions, causing material fragmentation (European Space Agency (ESA) Space Debris Office, 2022). Travelling at velocities of up to 15 km/s, MMOD poses a significant threat to manned and unmanned spacecraft (Cwalina et al., 2015). The extent of tracked debris populating Low Earth Orbit (LEO, orbit period < 128 min) has significantly increased since the 1960s, as shown in Figure 1 and detailed in The European Space Agency's (ESA) most recent annual Space Environment Report. Currently, ESA statistically estimates a vast space debris count of 130 million objects in orbit

*Corresponding author: f.teixeira-dias@ed.ac.uk (F. Teixeira-Dias). Email addresses: k.r.fowler@ed.ac.uk (K. Fowler)

with an approximate size range of 1 to 10 mm, regardless of object category (European Space Agency (ESA), 2023). Although the exact size distribution of debris in Figure 1 is not given in the ESA's report, the debris/object categories given are indicative of an approximate range of sizes. The US Space Surveillance Network catalogue covers objects larger than 5 − 10 cm in LEO, and from 30 cm to 1 m at geostationary (GEO) altitudes. Only a small fraction are intact, operational satellites today (European Space Agency (ESA) Space Debris Office, 2022).

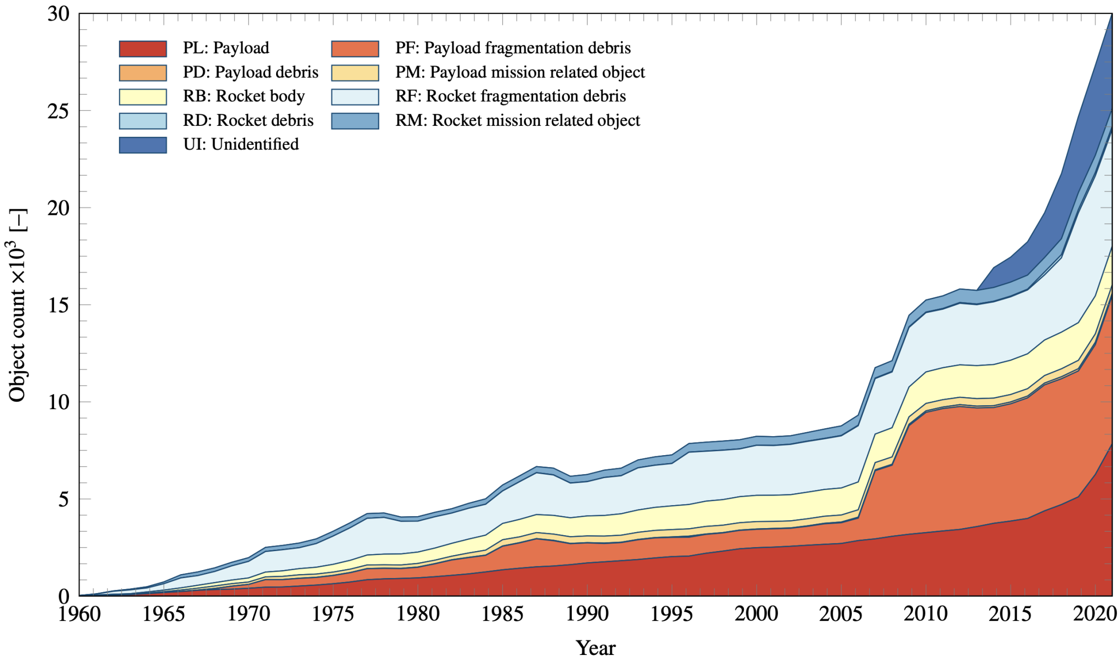

Figure 1: Evolution of number of objects in geocentric orbit since 1960, grouped by orbital debris object class (European Space Agency (ESA) Space Debris Office, 2022).

At hypervelocity, impacted structures experience characteristic failure phenomena, typically dependent upon the geometry and material composition of the debris impactor and shield (Signetti and Heine, 2022). The term hypervelocity refers to the hydrodynamic regime experienced at velocities greater than the wave propagation velocity through a solid medium (e.g. approximately 5-6 km/s for Aluminium targets) (Zukas et al., 1992).

Effective lightweight passive shielding technology, required to counter the damaging effects of MMOD, has developed since the Whipple shield was first suggested by Whipple (1947), traditionally consisting of an aluminium bumper plate and a rear plate, separated by a gap (stand-off distance), as shown schematically in Figure 2. The front bumper plate is a sacrificial layer designed to fragment the debris particle upon impact and undergo perforation. This creates a cloud of smaller particles consisting of solid, liquid and vapour components, and dissipates the kinetic energy of the debris particle (Eric, 2009). Individual fragmented debris particles have less kinetic energy and therefore significantly lower potential to cause catastrophic damage. The debris cloud disperses within the stand-off distance, increasing the impacted area on the rear wall, distributing momentum over a wider area. The rear wall is required to withstand the fragmented debris cloud upon impact to protect spacecraft from damage due to impulsive loading (see Figure 2). Complete perforation, spalling and tearing can occur as a result of debris cloud impact on the rear wall due to inadequate protection properties (Eric, 2009). Efficient protection against MMOD is therefore required to counter the complex phenomena and characteristic failure mechanisms observed at hypervelocity.

With the vast increase in MMOD in recent years and the prospect of increased space travel in the future, it is vital that more research is conducted into the development of efficient, lightweight shielding technology to protect spacecraft against hypervelocity impacts (HVI). Numerical modelling allows for the optimisation of spacecraft shield design, and helps reduce the cost of experimental test campaigns.

Subsequent to the initial design of the Whipple shield, alternative configurations have been developed to optimise lightweight shielding designs to maximise energy absorption characteristics. Consideration of energy absorption

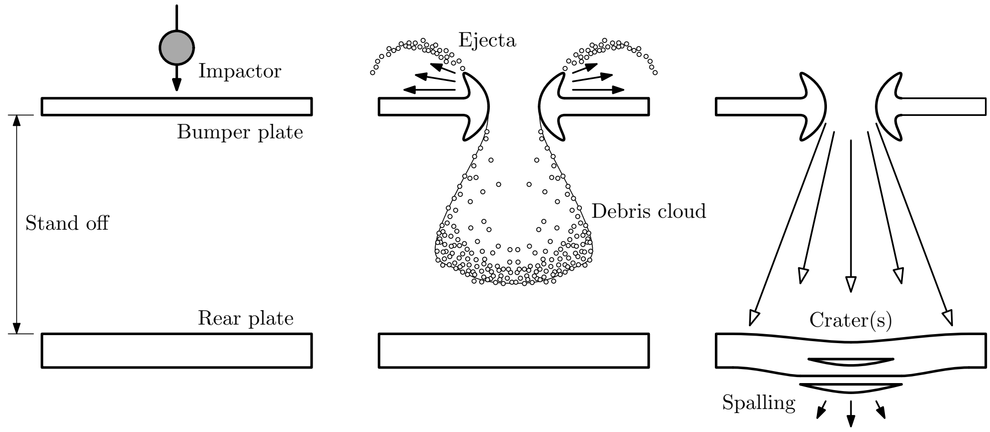

Figure 2: Traditional Whipple shield design and protection effect upon impact from MMOD particle (reprinted from Fowler and Teixeira-Dias (2022), licensed under CC BY 4.0).

properties in shield design is critical in minimising potentially catastrophic damage to spacecraft (Qu et al., 2020). Alternative shield configurations include the Stuffed Whipple shield (Figure 3a), the aluminium foam sandwich Whipple shield (Figure 3b), and numerous other hybrid multi-shock designs (Cherniaev and Telichev, 2016; Eric, 2009; Fowler and Teixeira-Dias, 2022).

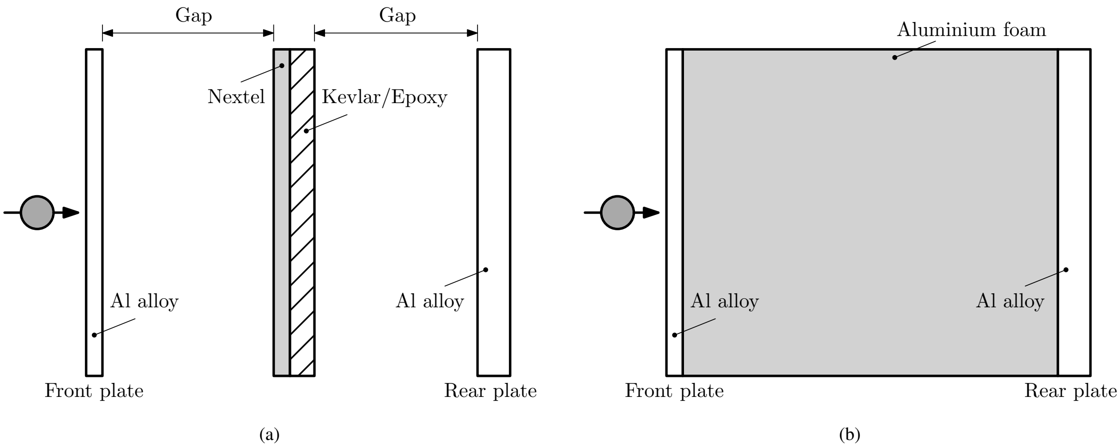

Figure 3: Alternative Whipple shield configurations: (a) stuffed Whipple shield and (b) foam sandwich Whipple shield (Cherniaev and Telichev, 2016) (reprinted from Fowler and Teixeira-Dias (2022), licensed under CC BY 4.0).

Studies into the shield configuration and material selection within multi-layered shield design have yielded particularly positive results in comparison with monolithic shields (Wan et al., 2013). White et al. (2003) found that for impact velocities above 7 km/s, the addition of Kevlar-epoxy layers to a carbon fibre reinforced polymer (CFRP) was beneficial in terms of decreasing the total momentum in the witness plate placed behind the shield design during experimental testing to capture any residual effects post impact. For impact velocities of $1-3$ km/s, outwith the hypervelocity regime, minimal improvement was seen compared with a monolithic CFRP plate, however less delamination effects in the CFRP plate were recorded as a result of adding the Kevlar-epoxy layers. A clear difference in the impact behaviour was observed between high velocity ($1-3$ km/s) and hypervelocity (> 7 km/s) regimes.

Multi-layer aluminium and ultra-high molecular weight polyethylene (UHMWPE) fibre laminates have also proven to provide good protection properties against HVI. Qu et al. (2020) found that the multi-layered Aluminium/UHMWPE designs out-performed monolithic alternative configurations. Optimal configurations were proposed by placing materials with a comparatively high strength and hardness on the impact side of the stacked layup. This configuration was found to be optimal in terms of anti-penetration performance. Three configurations were implemented in terms of aluminium/UHMWPE layup within this study. These authors also observed that decreasing the number of layers in the stacking sequence (and therefore the number of material interfaces) for the same total shield thickness, increased the penetration resistance of the laminate design as decreasing the laminate thickness also decreased the shear and bending stiffness for the individual laminates. Additionally, it was determined that multi-layer stacked ply configurations presented better results than the corresponding multi-layer spaced ply (i.e. with gaps between plies), in terms of depth of penetration (DOP). The addition of air gaps between plies causes a decrease in the compressive stress wave amplitude upon impact. Compressive stress waves are partially reflected within the shield material to form tensile stress waves at the rear surface of the ply when two materials of different densities are adjacent. This effect is eliminated with the addition of air gaps, resulting in lower compressive wave amplitudes.

Similar results in terms of the advantages of multi-layer shield design were observed by Slimane et al. (2021) using a honeycomb sandwich panel reinforced with a bi-layer ceramic facesheet (B_4C)/aluminium (Al 7075-T6). The results of HVI numerical modelling showed increased energy dissipation capabilities of the facesheet design owing to the combination of crushing/brittle fracture instigated by ceramic layers, and the high tensile strength and large deformation conferred by the aluminium layers. The proposed bi-layer facesheet design improved shielding performance in terms of energy absorption compared with a mono-layer (Al 7075-T6) design. Additionally, the bi-layer face sheet was more effective than alternative honeycomb designs, indicating potential for this hybrid bi-layer shielding design.

Extensive research has been carried out into the optimisation of fibre-metal laminates (FML) predominantly for aerospace applications within a relatively low velocity range. Aramid, glass and carbon fibre reinforced aluminium laminates make use of both the fibre and metal properties to optimise design for specific applications (Sinmazçelik et al., 2011; Soltani et al., 2011). Superior mechanical properties have been observed for FML compared with aluminium alloys and traditional composite materials. This includes a high impact resistance due to plastic deformation of metal plies, and high energy absorption capacity as a result of shear failure in the metal plies and localised fibre fracture (Sinmazçelik et al., 2011). Ply sequence plays an important role in the energy absorption characteristics of laminate structures (Baluch et al., 2013). Figure 4 shows the composition of an FML consisting of alternating aluminium and glass fibre composite layers (GLARE) (Zhong and Joshi, 2015).

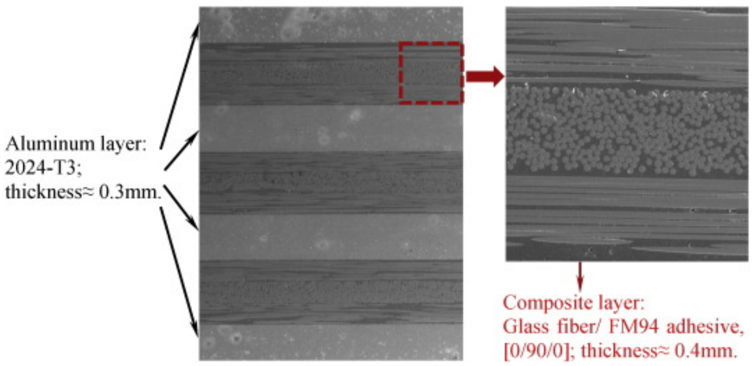

Figure 4: GLAss REinforced laminate (GLARE) composite layers (reprinted from Zhong and Joshi (2015), with permission from Elsevier).

Research on FML optimisation has recently been extended to HVI applications. FML configurations were analysed by Wan et al. (2013) in terms of the free surface velocity profile (the residual impact velocity recorded on the back surface of the target plate) and peak shock stresses. These authors found that introducing a higher number of plies was effective in reducing peak shock stresses. The steady state velocity plateau for FML configurations was found to be lower than for the monolithic designs due to a combination of the metal deformation and reduction in shock stresses due to the presence of fibre composite ply. This agrees with the work of Baluch et al. (2013) in which deformation and fibre fracture are highlighted as being key failure mechanisms under HVI.

The optimisation of shield design for HVI is a problem with high dimensionality, suited to advanced computational approaches such as machine learning. Based on a feature importance ranking study performed by Ryan et al. (2022), the most influential variables with regards to Whipple shield performance include: impact velocity, rear wall thickness, projectile diameter and bumper thickness. Despite contribution of numerous other design variables, these four were deemed most important and should therefore inform the optimisation focus of further shield design. Genetic Algorithm (GA) optimisation is an advantageous approach in that it allows for multi-variable optimisation directly based on simulation results, expanding the scope of shield design with complexity otherwise difficult to achieve.

GA optimisation approaches have been used by Arhore and Yasaee (2020) to develop advanced FML shielding for low impact velocity (10 m/s, outwith the hypervelocity regime) to optimise the FML layup, based on material, individual ply thickness and fibre orientation, reaching an 18% increase in the specific energy absorption of the shield. The improvement in protection properties as a result of the GA optimisation shows potential for these techniques in the development of more efficient shielding systems, including in space applications where impact velocities are orders of magnitude higher.

The development of shielding technology using multi-objective optimisation was also explored by Buyuk et al. (2008), with the aim of reducing the total areal density and minimising the internal energy at a pressure wall placed behind a Kevlar-Nextel shield. The proposed optimisation algorithm led to improved efficiency shield design, by varying the thickness and position of the Kevlar and Nextel layers. Further work by Kim et al. (2012) has been conducted on coupled FEM-SPH numerical techniques to develop aluminium Whipple shielding technology. Multi-objective optimisation was implemented to reduce shield mass and maximise stiffness properties. Optimisation was achieved by varying the Whipple shield plate thickness and stand-off distance, demonstrating that the combination of multi-objective optimisation and coupled FEM-SPH modelling techniques is an effective method of shield design optimisation.

Previous work on HVI shielding design, including the implementation of adaptive coupled FEM-SPH numerical methods, and the use of multi-layer FML is somewhat limited. Adaptive coupled FEM-SPH modelling, initially proposed by Johnson (1994) has since been studied to implement and improve the coupling algorithm. However, only a recent development has allowed for efficient HVI modelling using complex materials, owing to the work conducted by He et al. (2020) in using Johnson-Cook and maximum tensile strength failure criteria to improve the adaptive coupled FEM-SPH algorithm (Zhang et al., 2022).

The combination of the efficiency and accuracy of adaptive coupled FEM-SPH modelling techniques for HVI applications, and the effectiveness of FML designs in terms of efficient energy absorption due to combined failure modes, has significant potential in further optimisation of shield design. Combining these aspects with a multi-objective optimisation GA would allow for efficient optimisation of FML under HVI, leading to more effective shielding technology, which is the main aim of the research here proposed.

Section 2 below presents a theoretical overview of the adaptive coupled FEM-SPH numerical modelling techniques implemented, the material models used, and a numerical validation study against experimental results by Wan et al. (2013). A shield design optimisation solution is then presented in Section 3 based on GA optimisation methods.

2. Numerical and constitutive modelling

The hybrid shield configuration and numerical model shown schematically in Figure 5 is developed and validated based on the experimental work of Wan et al. (2013). 1 mm thick layers of Aluminium (AL2024) and CFRP (T300 woven-fabric) were alternated to form a 5 mm thick target plate consisting of 5 plies with an areal density of 11.48 kg/m^2. Using areal density allows the research to focus on optimising for total mass of the shield, regardless of its size. The Mylar projectile is modelled as a thin disk with 10 mm diameter and a thickness of 0.1 mm, to accurately represent the exploding foil experimental technique implemented by Wan et al. (2013). This representation of HVI is considered adequate given the limited published experimental results currently available.

2.1. Numerical modelling

Smoothed particle hydrodynamics (SPH) is a discrete particle-based meshless modelling technique typically used for fluid simulation problems (Hayhurst and Clegg, 1997). It is, however, also extensively used in HVI modelling due to the observed fluid-like impact behaviour of solids structures at these impact regimes (Cherniaev and Telichev, 2015). Mesh-based modelling methods such as the Finite Element Method (FEM) are prone to element distortion and negative volume effects as a result of the large deformations experienced upon hypervelocity impact (Zhao et al., 2028). Therefore, SPH methods are well suited to model the high strain rate loading of hypervelocity phenomena.

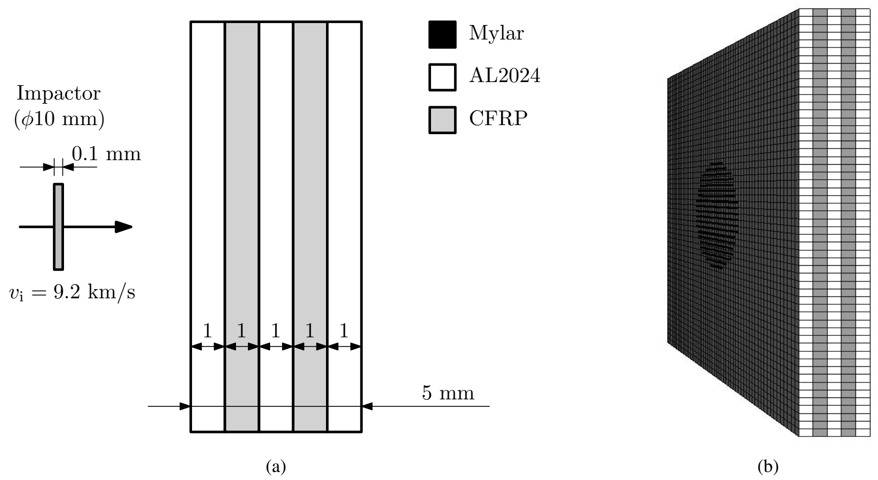

Figure 5: Shield design optimisation model: (a) schematic diagram of numerical model configuration for validation with experimental results by Wan et al. (2013) and (b) FE/SPH model highlighting discretisation of impactor (SPH particles) and plies (finite elements).

Previous work on SPH modelling of fibre composites by Riedel et al. (2006) discusses the development of detailed predictive simulations to capture complex damage failure modes as a result of HVI. This includes delamination and directional plasticity modelling within laminate structures. Clegg et al. (2006) have also developed SPH numerical techniques to accurately replicate experimental hypervelocity impact events by including orthotropic non-linear damage and non-linear shock effects, both critical factors in accurately representing hypervelocity phenomena.

SPH methods can however be computationally expensive compared with alternative mesh-based Lagrangian methods. To address this, adaptive coupled Finite Element Method — Smoothed Particle Hydrodynamic methods (FEM-SPH) have been developed to combine the computational efficiency of FEM methods and the meshless characteristics of SPH modelling. Adaptive coupled FEM-SPH methods perform well in terms of the accuracy of debris cloud data. Additionally, the mesh sensitivity for FEM-SPH methods is advantageously low, resulting in a further increase in modelling efficiency (Zhang et al., 2022). Despite these methods being currently in the development stage, numerical studies carried out by Zhang et al. (2022) concluded that they can be more suitable for HVI modelling over alternative methods such as SPH, based on mesh sensitivity parameters, comparisons with experimental results and numerical error analyses.

The adaptive coupled FEM-SPH method was implemented within LS-DYNA to model each ply. The models are discretised using a finite element mesh, to which SPH particles are constrained before failure. Each discrete ply was discretised with solid 8-node reduced integration elements (finite element C3D8R in LS-DYNA). SPH particles were separately defined for each ply, linked to the corresponding ply mesh (Livermore Software Technology Corporation (LSTC), 2012; Zhang et al., 2022). When the failure criteria is reached, as described within the damage models detailed in the following paragraphs for aluminium and CFRP materials, the original elements are deleted and converted into SPH particles, as shown schematically in Figure 6 (He et al., 2020). These discrete particles inherit volume and material properties at the time of failure. Activated SPH particles are coupled with the remaining pre-converted mesh for further calculation (Zhang et al., 2022).

The 10 mm diameter and 0.1 mm thickness Mylar projectile was modelled with SPH particles to better account for extreme material distortions. The dimensions used ensure the mass and kinetic energy of the projectile in the numerical models is consistent with the experimental set-up. An initial impact velocity v_0 = 9.2 km/s was applied perpendicular to the target plate, representative of orbital debris (Eric, 2009).

2.2. Material modelling

The Johnson-Cook (JC) constitutive law is commonly used to describe isotropic metallic materials for high strain-rate applications where work-hardening, strain-rate hardening and thermal softening need to be considered (Salvado

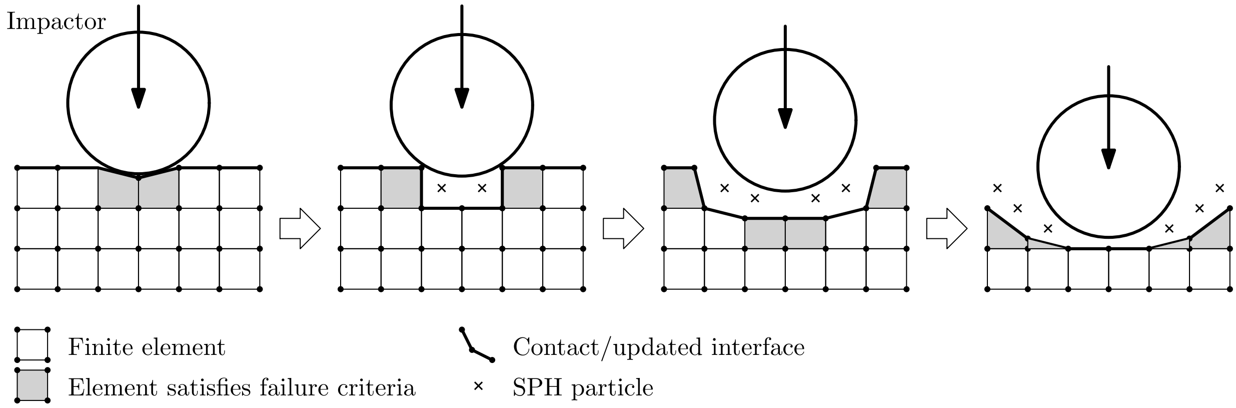

Figure 6: Generic schematic representation of adaptive coupled FEM-SPH modelling (adapted from He et al. (2020)).

et al., 2017; Slimane et al., 2021). This constitutive equation can be described as,

$$\bar{\sigma} = \left[A + B\left(\bar{\varepsilon}^{\mathrm{pl}}\right)^{n}\right]\left[1 + C\ln\left(\frac{\dot{\bar{\varepsilon}}^{\mathrm{pl}}}{\dot{\bar{\varepsilon}}_{0}^{\mathrm{pl}}}\right)\right]\left[1 - (T^{*})^{m}\right] \tag{1}$$

where $\bar{\sigma}$ is the flow stress, $\bar{\varepsilon}^{\mathrm{pl}}$ is the equivalent plastic strain, $\dot{\bar{\varepsilon}}^{\mathrm{pl}}$ is the equivalent plastic strain rate, n is the strain hardening exponent, A, B, C and m are experimentally determined material constants (Wang and Shi, 2013), and $T^{*} = (T - T_{\mathrm{t}})/(T_{\mathrm{m}} - T_{\mathrm{t}})$ is the non-dimensional homologous temperature, where T, T_{t} and T_{m} are the current, transition and melting temperatures, respectively. The JC failure/damage model, which also incorporates the effects of plasticity, temperature and strain-rate, is described by

$$\bar{\varepsilon}_{\mathrm{D}}^{\mathrm{pl}} = \left[D_1 + D_2 \exp\left(-D_3\eta\right)\right]\left[1 + D_4 \ln\left(\frac{\dot{\bar{\varepsilon}}^{\mathrm{pl}}}{\dot{\bar{\varepsilon}}_{0}}\right)\right]\left(1 + D_5 T^{*}\right) \tag{2}$$

where D_i $(i = 1, \ldots, 5)$ represent the damage parameters. η is the stress triaxiality, referring to the ratio of pressure to the equivalent stress. Damage occurs when $D = \sum \bar{\varepsilon}_{\mathrm{D}}/\bar{\varepsilon}_{\mathrm{D}}^{\mathrm{pl}} \geq 1$, where $\bar{\varepsilon}_{\mathrm{D}}$ is the Johnson-Cook flow strain. The damage evolution relationship defines the subsequent material stiffness degradation properties (Wang and Shi, 2013). The material properties for the aluminium alloy AL2024 target plates are listed in Table 1, together with the Mie-Grüneisen parameters.

The Mylar projectile is a polymeric material that exhibits compressible fluid-like behaviour under high strain-rate loading. The impact pressure dominates compared with material mechanical properties and consequently an EoS is all that is required to model the material behaviour (Zhao et al., 2028). Therefore the non-linear Mie-Grüneisen Equation of State (EoS) is used to describe the evolution of pressure, internal energy and density, which is critical when considering HVI due to the high strain-rates and shock wave mechanics. The `*MAT_NULL` keyword in LS-DYNA was required to define the material density. This EoS is described as

$$p = \frac{\rho_0 c^2 \mu \left[1 + \left(1 - \frac{\gamma_0}{2}\right)\mu - \frac{a}{2}\mu^2\right]}{\left[1 - (S_1 - 1)\mu - S_2\frac{\mu^2}{\mu+1} - S_3\frac{\mu^3}{(\mu+1)}\right]} + (\gamma_0 + a\mu)\,U \tag{3}$$

where p is the pressure, $\mu = (\rho/\rho_0 - 1)$ is the relative density, U is the internal energy, c, S_1, S_2 and S_3 are material constants, and γ_0 is the non-dimensional Grüneisen constant with the associated volume correction factor a. Assuming pressure is adequately described by a first order constant S_1, then $S_2 = S_3 = 0$. The Mie-Grüneisen parameters for Mylar are also listed in Table 1.

Four failure modes are considered when describing damage in the composite material: delamination and tensile, compressive and transverse shear failure (Giannaros et al., 2019; Tepeduzu and Karakuzu, 2019). The failure criteria

Table 1: Material properties for the Johnson-Cook (JC) constitutive law (AL2024), Johnson-Cook damage model parameters (AL2024) (Venkatesan et al., 2017) and Mie-Grüneisen equation of state parameters (AL2024 and Mylar) (Nor et al., 2020; Zhao et al., 2028).

Elastic properties (AL2024)			
Shear modulus, G	26.9	GPa	
Poisson's ratio, ν	0.3	–	
Elastic modulus, E	69.9	GPa	
JC constitutive model parameters (AL2024)			
A	167	MPa	
B	684	MPa	
n	0.551	–	
C	0.001	–	
m	0.859	–	
JC damage model parameters (AL2024)			
D_1	0.112	–	
D_2	0.123	–	
D_3	1.500	–	
D_4	0.007	–	
D_5	0.0	–	
Equation of state (AL2024, Mylar)			
	AL2024	Mylar	
Density, ρ	2785	1400	kg/m^3
Grüneisen constant, γ_0	1.97	0.76	–
S_1	1.4	1.56	–
Wave speed, c	5240	2270	m/s
Volume correction factor, a	0.48	0	–

used to predict these failure modes are based on damage plasticity theory to describe the stress-strain material response under loading.

Each woven orthotropic CFRP layer is modelled as a homogenised singular ply plate with equivalent perpendicular in-plane stiffness. Solid elements are used in order to more accurately capture the shock wave response in the through-thickness ply direction (Wicklein et al., 2008). Although consideration of through-thickness stress increases the modelling accuracy, it can reduce the computational efficiency (Yong et al., 2008). MAT 59 (`*MAT_COMPOSITE_FAILURE_SPH_MODEL`) is an orthotropic composite material model in LS-DYNA, where compressive, shear and delamination failure modes are considered as they are key failure modes for composite materials under HVI (Giannaros et al., 2019). The stress-strain deviatoric response and damage criteria adequately describe the material response, removing the requirement for an EoS for the composite material. The elastic and stiffness parameters for CFRP (T300 woven-fabric) are listed in Table 2.

Delamination failure between adjacent CFRP and AL2024 plies was modelled using a penalty-based tie-break contact algorithm suited to high deformation impact analysis to describe the contact between contact interfaces where debonding occurs when the following stress criterion is met (Rabiee and Ghasemnejad, 2022; Raza et al., 2021):

$$\left(\frac{\sigma_{\mathrm{n}}^2}{U_{\mathrm{n}}}\right)^2 + \left(\frac{\sigma_{\mathrm{s}}^2}{U_{\mathrm{s}}}\right)^2 = 1 \tag{4}$$

where σ_{n} is the normal stress, σ_{s} is the shear stress, U_{n} is the normal failure strength, and U_{s} is the shear failure strength. Tiebreaks can resolve penetration or overlapping of elements by either merging or separating the conflicting surfaces, without compromising the accuracy of the results (Raza et al., 2021). This approach removes the requirement

Table 2: Quasi-isotropic CFRP materials properties and damage model parameters (Zhang et al., 2015).

Elastic material properties									
Density [kg/m^3]	Elastic moduli [GPa]			Poisson's ratios			Shear moduli [GPa]		
ρ	E_{11}	E_{22}	E_{33}	ν_{12}	ν_{13}	ν_{23}	G_{12}	G_{13}	G_{23}
1600	41	41	3.4	0.03	0.23	0.23	3.6	2.5	2.5

Damage model parameters								
Tensile strengths [MPa]			Compressive strengths [MPa]			Shear strengths [MPa]		
X_T	Y_T	Z_T	X_C	Y_C	Z_C	S_{12}	S_{23}	S_{13}
351	351	51	402	402	149	171	54	54

for additional layers of elements at the ply interfaces. The cohesive interface uses the Dycoss Discrete Crack Model for defining tiebreak contacts, incorporating crack opening damage (mode I) and in-plane shear damage (mode II). The tiebreak properties are based on resin initiation stresses (U_{n} and U_{s}), and critical strain energy release rates (G_{IC} and G_{IIC}), corresponding to damage modes I and II, respectively. The tiebreak parameter data listed in Table 3 approximates the resin contact between metal-composite and composite-composite ply interfaces based on experimental data for CFRP resin interaction (Al-azzawi et al., 2017).

Table 3: Ply interface tiebreak parameters (Al-azzawi et al., 2017).

Interlaminar fracture strengths [J/m^2]		Normal	Failure strengths [MPa]	
Mode I, G_{IC}	Mode II, G_{IIC}	stiffness [GPa], N	Normal, U_{n}	Shear, U_{s}
450	1000	25	40	40

2.3. Convergence and validation

A detailed convergence analysis was conducted to optimise the FE mesh and SPH particle densities. Figure 7a shows the dependency of the free surface velocity on the mesh density for the target ply mesh, with corresponding trend lines. A converging solution was observed as the mesh reaches a density of approximately 1.8 elements/mm. The accuracy of the free surface velocity results was also analysed in terms of SPH density (i.e. the number of SPH particles per unit of linear distance) of the projectile as shown in Figure 7b. An SPH density of 2 particles/mm was used as it was observed that there was no significant change in the free surface velocity above this value, as can be seen in Figure 7b.

The experimental observations by Wan et al. (2013) were used to validate the proposed numerical model. Experimental data for hypervelocity impact with the particular combination of materials used in this research is extremely limited and as such the free surface velocity is used as the main validation parameter.

The results in Figure 8 show the history of the free surface velocity v_{r} for both the numerical modelling and the experimental results. A 30% difference is observed between the numerical simulation and experimental free surface peak velocity, indicating that a higher shock wave stress is experienced (Wan et al., 2013). The numerical model therefore initially overestimates the shock wave stress within the target plate material. The steady state solution, however, remains close to the experimental data, with a 1.9% difference between the average experimental and the average numerical results for $0.6 < t < 2.6\ \mu$s.

Figure 9 shows a cross-sectional view of the numerical model of the hybrid shield at $t = 4\ \mu$s with labels added indicating examples of locations where plastic deformation, brittle fracture and delamination occur. Also shown are the finite elements where the brittle fracture criteria threshold has been met are converted SPH particles (red particles). It can be observed that the AL2024 plies dissipate energy mostly through plastic deformation, whereas the CFRP plies show wider evidence of brittle failure due to transverse shear stress, hence contributing to minimising the shock wave stress (Wan et al., 2013). Delamination is also visible between metal and fibre laminates as a result of interlaminar

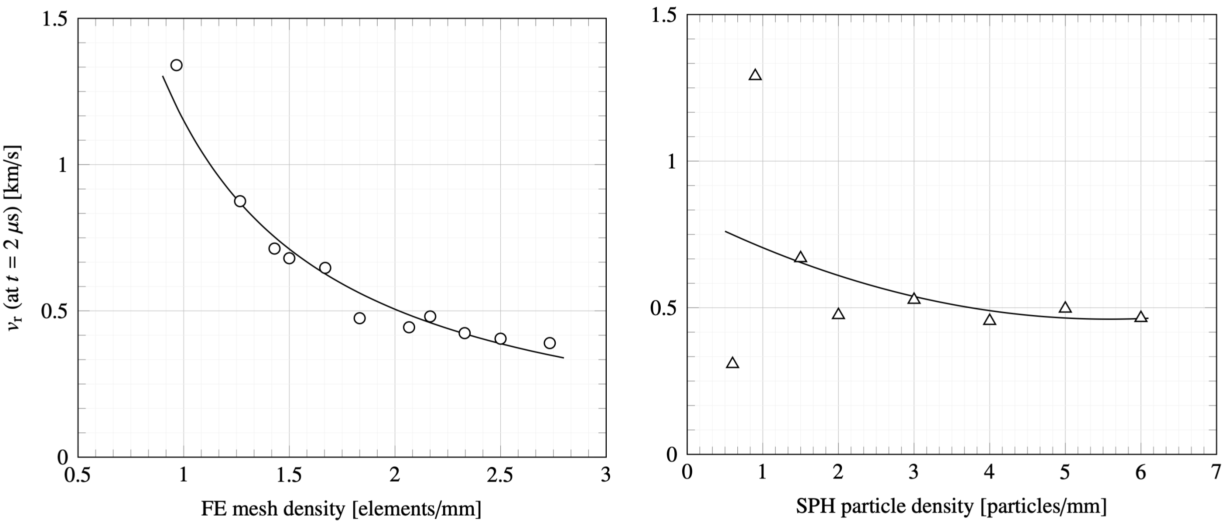

(a) (b)

Figure 7: Numerical maximum free surface velocity v_r at the rearmost target plate at $t = 2$ μs against: (a) FE mesh density and (b) SPH particle density.

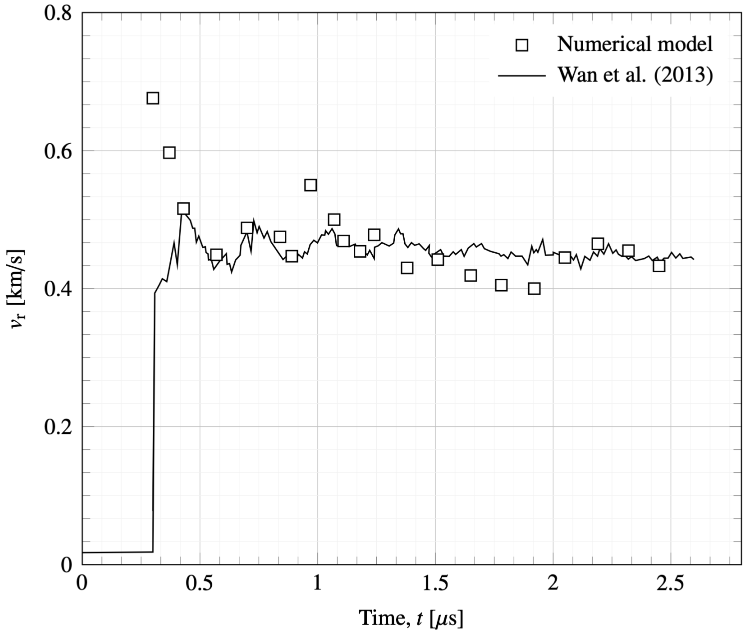

Figure 8: Numerical maximum free surface velocity v_r at the rearmost target plate and comparison with experimental results (Wan et al., 2013).

shear stress due to weak interfacial contact. The observed combination of failure and damage mechanisms agrees with the observations of Wan et al. (2013).

3. Shield design optimisation

The proposed hypervelocity shield design optimisation methodology is based on Direct Simulation-based Genetic Algorithm (DSGA) optimisation. This uses a GA in conjunction with direct simulation-based optimisation to solve multi-objective optimisation problems by iteratively running numerical simulations. The overarching aim of the GA

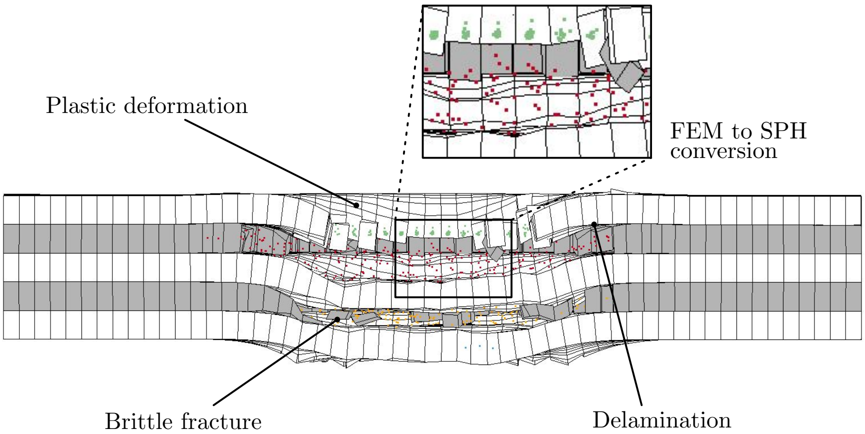

Figure 9: Cross-sectional view of the hybrid shield at $t = 4\ \mu$s, showing examples of plastic deformation, brittle fracture and delamination, and FEM to SPH conversion (red particles).

is to find a converged optimal solution within a given design space defined by a set of variables and constraints and this approach is implemented with LS-OPT to optimise a multi-variable MMOD hypervelocity impact shield design space. Each solution within the algorithm requires a numerical simulation to run (in LS-DYNA in this case), where the fitness is assessed based on the simulation results. DSGA optimisation is typically extremely computationally expensive due to the number of iterative simulations required to obtain convergence. This computational cost can be significantly reduced, however, with adaptive coupled FEM-SPH techniques providing an efficient simulation methodology. Within each optimisation iteration, multiple simulations are run simultaneously to compare fitness and increase the GA efficiency.

Based on the feature importance study performed by Ryan et al. (2022), this work uses a rear wall and bumper thickness-related parameter — the areal density of the shield — as the design optimisation constraint, allowing the design optimisation strategy to focus on the kinetic energy of a critical element of the shield: the rear plate. This modelling and optimisation approach also allowed the study and results to be validated with the work of Wan et al. (2013).

3.1. *Optimisation methodology*

The multi-objective optimisation was defined in terms of the objectives, variable parameters and constraints, as described in Table 4. Constraints are necessary to limit the design space. The proposed GA is implemented in LS-OPT, using the algorithm parameters detailed in Table 5.

Table 4: Objectives, variable parameters and constraints for the shield design multi-objective optimisation.

Objectives	Minimise the kinetic energy of the rearmost target ply (relative to the direction of impact) Minimise the total mass of the target plate (summation of individual ply mass)
Variables	Thickness of individual ply Material for each ply (AL2024, CFRP)
Constraints	Ply thickness constrained to ±40% of the original thickness (for each individual ply)

Table 5: GA parameters for the shield design multi-objective optimisation.

Parameter	Value
Population size	10
Number of generations	100
Mutation distribution	100
Mutation probability	0.1
Crossover distribution	10
Crossover probability	1.0

3.2. Optimisation results and discussion

The convergence of the Direct Simulation-based Genetic Algorithm (DSGA) optimisation is shown in Figure 10. Each data point in this figure represents the optimal solution from the set of 10 models for each iteration in terms of the independent objectives, the kinetic energy and mass outputs. The normalised kinetic energy of the rearmost target ply and the areal density of the shield are displayed against the number of iterations completed during the optimisation routine. It can be observed that the areal density (mass) of the target converges quickly from iteration 1 to 2, that is in only the first 20 simulations, with only minimal variation after iteration 2. The kinetic energy, however, converges at a slower rate, with the largest decrease also observed between the first 2 iterations and convergence by iteration 8, that is after 80 simulations.

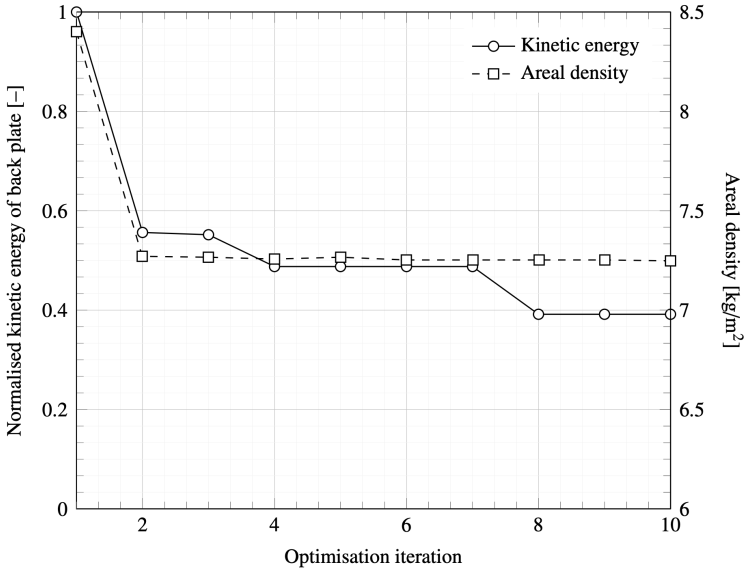

Figure 10: Convergence analysis of optimisation objectives: normalised kinetic energy of the rear plate and areal density of the shield.

The optimised results for the kinetic energy of the rear plate, areal density of the target and their relative differences are listed in Table 6. Objective weightings are used to analyse the results, which refer to the value of objectives with respect to each other, i.e. the ratio of the values of the kinetic energy objective to the mass objective (E_k:mass). This allows different designs to be compared and analysed for different situations, such as the kinetic energy dissipation being valued more highly than a reduction in mass. Weighting 100:0 indicates that the objective to minimise the mass is not considered, and therefore the problem becomes a single objective optimisation. The 90:10 and 50:50 weightings refer to the ratio of objectives, leading to a weighted trade-off between the results. The original configuration is included as a reference model, to allow for a comparison with the optimised solutions. The energy dissipation and the relative change in mass is displayed for each weighting with respect to the original configuration. The negative relative difference in the kinetic energy dissipation and the change in mass represents a reduction in the absolute value relative to the original value, resulting in an improved protection capability of the shielding configuration. The configuration of the material layers within the target plate, and the corresponding thickness of each layer is also listed in Table 6.

Table 6: Kinetic energy dissipation and change in shield areal density, highlighting a decrease in ply thickness (red) and a reduction in relative objectives (bold).

Weighting (E_k : mass)	**Material configuration**	**Ply thickness** [mm]	**Normalised kinetic energy**	**Areal density** [kg/m^2]	**Energy dissipation**	**Mass change**
	AL2024	1.00				
	CFRP	1.00				
Original	AL2024	1.00	0.3339	11.48	Reference	Reference
	CFRP	1.00				
	AL2024	1.00				
	CFRP	0.44				
	AL2024	1.89				
100 : 0	AL2024	0.97	0.0433	11.97	**−87.0%**	+3.7%
	CFRP	0.99				
	CFRP	1.09				
	CFRP	0.44				
	CFRP	1.90				
90 : 10	AL2024	0.97	0.1245	9.35	**−62.7%**	**−18.6%**
	CFRP	1.01				
	CFRP	0.92				
	CFRP	0.44				
	CFRP	1.90				
50 : 50	CFRP	0.97	0.6119	8.15	+83.2%	**−28.9%**
	CFRP	1.01				
	CFRP	0.92				

The material configuration for each optimised model increases in CFRP content as the value of the mass objective increases, due to the lower density material properties. The ply thickness for each optimised configuration remains within a 2% variation between the models of different objective weightings. The front ply is consistently 44% of the original ply thickness, the second ply is an average of 189.7% of the original thickness, and the final three plies remain within 9% of the original thickness. These values of ply thickness appear to be insensitive to changes in the kinetic energy dissipation and to changes in the mass objective weightings. The optimised ply thickness for weighting 100:0, where a mass reduction is not considered, indicates that the observed ply configuration is an attempt to solely reduce the kinetic energy of the back plate. The consistency in the ply thickness results across each objective weighting, where the mass is increasingly valued, indicates the importance of the given configuration in maximising the absolute value of negative kinetic energy dissipation. The results in Figure 11 show the absolute values of the normalised kinetic energy and areal density for each objective weighting.

An 87% decrease in the kinetic energy of the back plate is observed between the weighted objective configuration 100:0, and the original configuration. As a weight of zero is given to the mass objective, however, the mass increases by 3.7% when the optimisation leads to a decrease in the kinetic energy. The 90:10 configuration shows a decrease of 62.7% in the kinetic energy and an 18.6% decrease in the target mass. Although this configuration is not as efficient in terms of kinetic energy dissipation as the 100:0, it achieves a clear trade-off between objectives. The 50:50 configuration values the kinetic energy dissipation and the mass reduction objectives equally, resulting in a 28.9% decrease in the areal density of the shield. The kinetic energy, however, increases beyond the original solution, resulting in a 83.2% increase compared with the original configuration. In this case the trade-off between objectives has resulted in overcompensation when attempting to further decrease the mass. The kinetic energy is therefore sub-optimal and this configuration is not a valuable solution. It can therefore be determined that to minimise both the kinetic energy and the target mass, the results of objective weighting 90:10 should be used. This configuration presents an optimal solution for each objective criteria based on a suitably scaled trade-off.

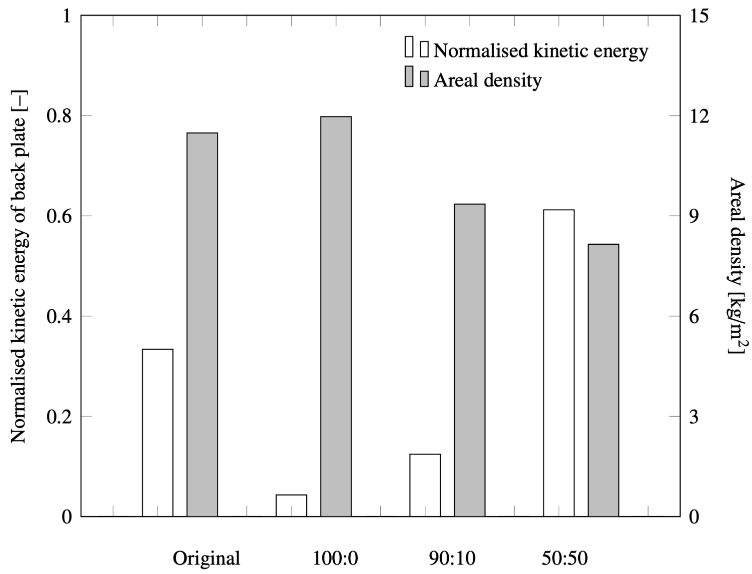

Figure 11: Normalised kinetic energy of the rear plate and areal density of target for original and optimised models (absolute values).

3.2.1. Pareto optimal solutions

Convergence towards a singular optimal solution is often not attainable with multi-objective GA optimisation due to the forced trade-off between parameters subject to contrasting objective functions (Ashby, 2000). Pareto optimality is used in conjunction with multi-objective optimisation to define a set of solutions for which the value of each solution is non-inferior within the set of optimal solutions, based on a weighted objective. Weighted objectives are used to determine the sensitivity of multiple objectives, as each weighted objective will have a different optimal solution.

The Pareto optimal solutions listed in Table 7 correspond to the observed results for each weighted objective shield configuration, as listed in Table 6. The Hyper-Radial Visualisation (HRV) plots for each objective weighting, also shown in Table 7, highlight the optimal Pareto solution for the specified weighting. These help visualise the value of each solution with respect to the alternative solutions, on a scale from 0 to 1 along the x-axis and y-axis. Indifference curves are included to indicate bands of equivalent value. A scaled representation of each highlighted solution for the corresponding objective weighting is also shown, where the top segment of each configuration represents the front impacted plate of the shield. A Pareto optimal frontier can be clearly observed for the 90:10 and 50:50 weighted solutions. This is displayed as a dashed red line on the respective HRV plots, indicating the varying non-inferior solutions for different objective weightings.

3.2.2. Shield configuration and damage analysis

Simulation results at $t = 0.8\ \mu$s are shown in Figure 12, for both the original and the optimised configurations. The SPH impactor and target plate particles have been removed to aid visualisation of the post impact target plate damage.

The original configuration shows a plastic response of the front impacted AL2024 ply and a brittle response of the second layer due to the high strain rate properties of the CFRP. The optimised results of the 100:0 configuration, weighted towards kinetic energy dissipation, include a thin CFRP plate followed by a relatively thick AL2024 plate (1:4.3 thickness ratio). Brittle fracture is observed on the front plate and plastic deformation in the AL2024 layers. The 90:10 reduced mass configuration displays similar damage as the 100:0 configuration as the layer configuration is similar. It appears that the reduction in kinetic energy dissipation compared with the 100:0 configuration is primarily due to the second CFRP ply replacing the AL2024 ply. This results in a shift in the dominant failure mechanism of the target plate, from plastic deformation energy absorption mechanisms to brittle fracture. The optimal configuration in terms of kinetic energy dissipation is a multi-layer combination of CFRP and AL2024, supported by the observations of Wan et al. (2013). The CFRP plate induces fragmentation of the impactor, reducing the shock stress, albeit dissipating less kinetic energy compared with alternative fracture mechanisms (Wan et al., 2013). The AL2024

Table 7: Optimised shield configurations with corresponding Pareto optimal plots. Red marker denotes the optimal solution for different kinetic energy to mass objective weighting and solid red line are the Pareto optimal frontiers. Aluminium plies shown in white, CFRP in grey and layer thicknesses are shown to scale.

Weighting (E_{k}:mass)	**Configuration** (scaled) (AL2024: white, CFRP: grey)	**Pareto optimal solutions** (optimal solution: red marker)
100:0	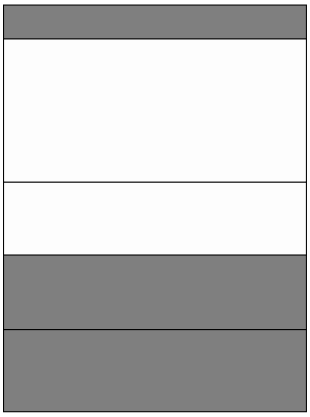	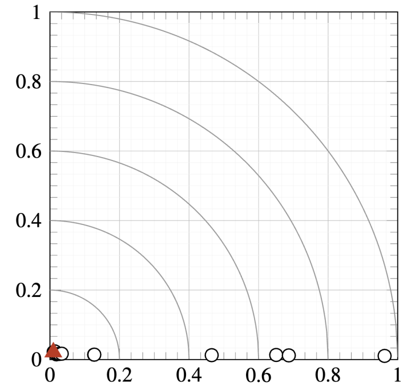
90:10	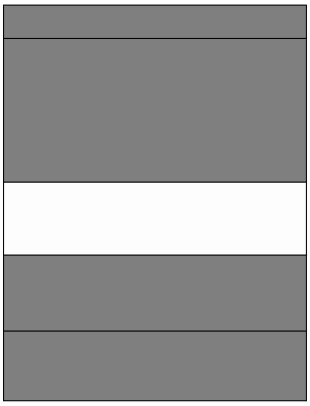	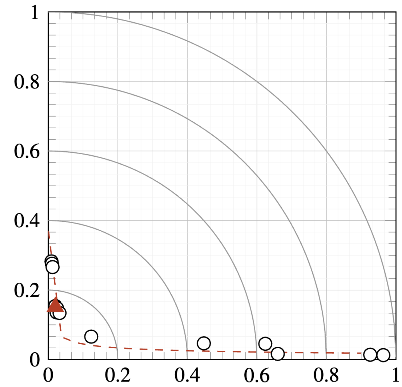
50:50	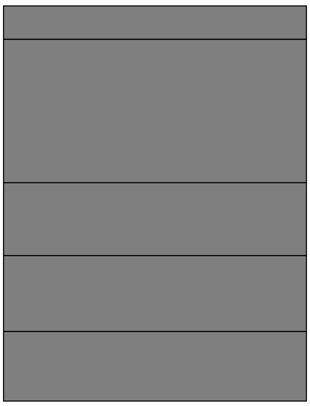	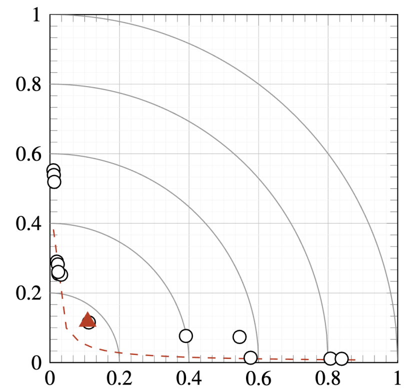

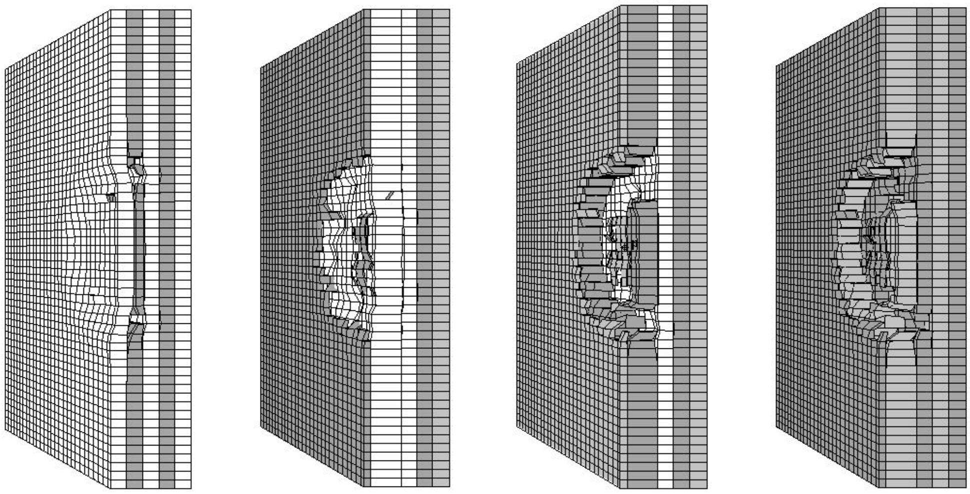

(a) Original (b) 100:0 (c) 90:10 (d) 50:50

Figure 12: Simulation results highlighting damage of (a) original and (b–d) optimised configurations at $t = 0.8\ \mu$s (aluminium plies shown in white and CFRP in grey, alternating shades of grey are used to represent discrete CFRP plies).

ply undergoes plastic deformation, contributing to the absorption of impact kinetic energy. The order in which these failure mechanisms develop is critical in kinetic energy dissipation for HVI, as previously confirmed by Qu et al. (2020). The relative thickness of the first 3 layers is also critical, with a thin layer of CFRP followed by a thick layer of AL2024 being the optimal solution in terms of energy dissipation. The poor results regarding the kinetic energy dissipation of the 50:50 weighted configuration are likely due to the absence of the plastic deformation provided by the AL2024 layer(s).

3.3. *Impact velocity case study*

The proposed optimisation of shield design method is used to analyse the effect of the projectile impact velocity, with the aim of providing an indication of the range of scenarios for which the optimised solution performs effectively. The impact velocity, and thus the kinetic energy E_{abs}, is one of the most influential factors for shield modelling in terms of the contribution to model outputs, based on feature importance ranking methods (Ryan et al., 2022). This factor, which can vary enormously and has a significant effect on the energy absorbed by the shield, is $E_{\mathrm{abs}} = m_{\mathrm{p}}(v_{\mathrm{i}}^2 - v_{\mathrm{r}}^2)/2$, where v_{i} is the initial impact velocity, v_{r} is the post impact residual velocity, and m_{p} is the mass of the projectile. To isolate the effects of the impact velocity v_{i} in the analyses, all remaining model parameters were kept unchanged relative to the original model configuration. Pareto optimal solutions were obtained for objective weightings 90:10 and 50:50, for each model and the results in Figure 13 show the relationship between the kinetic energy dissipation and projectile impact velocity. The negative kinetic energy dissipation in Figure 13 indicates a reduction in the absolute kinetic energy compared with the original design, whereas the positive kinetic energy dissipation indicates an increase in kinetic energy. The 50:50 case shows an unclear trend between 0 and 2 km/s. This is likely to be caused by the interaction of elastic waves within the target layers, due to the different mechanical impedances. In the hypervelocity regime, this relative difference is explained in terms of the trade-off between objective functions as previously discussed. For impact velocities within and below the hypervelocity transition region (below approximately 5 km/s), the results consistently show a significant increase in kinetic energy dissipation, indicating a higher absolute kinetic energy.

The analysis covers a wide range of velocities to explore the effects of the kinetic energy of the impact over different velocity regimes. The change in regime to high-velocity impact is estimated by the upper and lower values of the wave propagation velocity c_0 through the target layer materials, which can be estimated as $c_0 = \sqrt{E/\rho}$, where E and ρ are the layer material elastic modulus and density, respectively.

As expected, a clear transition in the impact behaviour of the optimised plates can be observed in this region. Significant levels of kinetic energy dissipation are observed below the transition region, with minimal energy dissipation

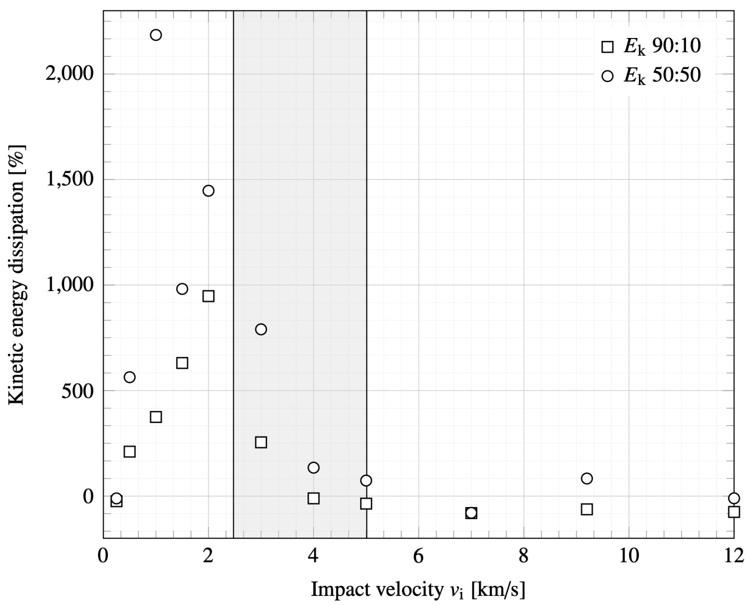

Figure 13: Kinetic energy dissipation of weighted Pareto optimal solutions against impact velocity v_i, with the region between the wave propagation velocities for AL2024 (upper bound) and CFRP (lower bound) highlighted in grey.

happening in the hypervelocity impact region. The transition to hypervelocity regime, highlighted in Figure 13, agrees with the kinetic energy dissipation results obtained for the optimal solutions. Although the results remain consistent above the transition region, the behaviour changes below this region, indicating that shield optimisation is more sensitive to the impact velocity within the high-velocity regime, as apposed to the hypervelocity regime. As both 90:10 and 50:50 weighted optimised configurations mainly consist of CFRP ply, the wave propagation velocity is likely to be closer to the lower bound, which agrees with the rapid decrease in the kinetic energy dissipation as the impact velocity increases between approximately 2 and 4 km/s.

4. Concluding remarks

An adaptive coupled FEM/SPH numerical model is developed and implemented in LS-DYNA, and validated against the experimental results from Wan et al. (2013). An AL2024/CFRP hybrid configuration is proposed, taking advantage of multiple damage/fracture mechanisms to increase the energy absorption properties of the shield. A multi-objective optimisation is proposed and carried out on the validated model, with the aim of minimising the kinetic energy of the back plate of the target and its areal density (i.e. total mass). The optimisation was conducted based on variable ply thickness, material parameters and ply arrangement. Pareto optimal solutions were obtained for different objective weightings, defined by the ratio of value of the energy dissipation to mass reduction objectives. The shield design optimisation results show that with a weighted objective of 90:10, the kinetic energy of the back target plate decreases by 62.7% and the shield mass reduces by 18.6%, compared with the original configuration. Alternative configurations displayed sub-optimal results based on a trade-off between objective functions. The 100:0 model achieved a 87.0% decrease in kinetic energy, however the mass increased by 3.7% as a result whereas the 50:50 model reduced the mass by 28.9% and increased the kinetic energy by 83.2%. The effect of impact velocity on the kinetic energy dissipation of shield configurations is also discussed based on the transition between high-velocity and hypervelocity impact regimes.

Acknowledgement

The authors acknowledge the support given to this project by the Engineering and Physical Sciences Research Council (EPSRC, United Kingdom) [grant: EP/W524384/1].

The authors would also like to acknowledge Dr Francesca Letizia and Mr Stijn Lemmens from the European Space Agency and the European Space Operations Centre (ESA/ESOC) for facilitating the Micro-Meteoroid and Orbital Debris (MMOD) data.

References

Al-azzawi, A., Kawashita, L. and Featherston, C. (2017), 'Buckling and postbuckling behaviour of glare laminates containing splices and doublers. Part 2: Numerical modelling', *Compos. Struct.* **176**, 1170–1187.

Arhore, E. and Yasaee, M. (2020), 'Lay-up optimisation of fibre–metal laminates panels for maximum impact absorption', *J. Compos. Mater.* **54**(29), 4591–4609.

Ashby, M. (2000), 'Multi-objective optimization in material design and selection', *Acta Mater.* **48**(1), 359–369.

Baluch, A., Park, Y. and Kim, C. (2013), 'Hypervelocity impact on carbon/epoxy composites in low earth orbit environment', *Compos. Struct.* **96**, 554–560.

Buyuk, M., Kurtaran, H., Marzougui, D. and Kan, C. (2008), 'Automated design of threats and shields under hypervelocity impacts by using successive optimization methodology', *Int. J. Impact Eng.* **35**(12), 1449–1458.

Cherniaev, A. and Telichev, I. (2015), 'Meso-scale modeling of hypervelocity impact damage in composite laminates', *Compos. B. Eng.* **74**, 95–103.

Cherniaev, A. and Telichev, I. (2016), 'Weight-efficiency of conventional shielding systems in protecting unmanned spacecraft from orbital debris', *J Spacecr. Rockets* **54**(1).

Clegg, R., White, D., Riedel, W. and Harwick, W. (2006), 'Hypervelocity impact damage prediction in composites: Part I — material model and characterisation', *Int. J. Impact Eng.* **33**(1–12), 190–200.

Cwalina, C. D., Dombrowski, R. D., McCutcheon, C. J., Christiansen, E. L. and Wagner, N. J. (2015), 'MMOD puncture resistance of EVA suits with shear thickening fluid (STF) — Armor absorber layers', *Procedia Eng.* **103**, 97–104.

Eric, L. (2009), *Handbook for Designing MMOD Protection*, Astromaterials Research and Exploration Science Directorate Human Exploration Science Office NASA Johnson Space Center.

European Space Agency (ESA) (2023), 'Space debris by the numbers', `https://www.esa.int/Space_Safety/Space_Debris/Space_debris_by_the_numbers`. Accessed 5 April 2023.

European Space Agency (ESA) Space Debris Office (2022), European Space Agency's Annual Space Environment Report, Report ESA/ESOC-SRO(2022)401, European Space Operations Centre (ESOC), Darmstadt, Germany.

Fowler, K. and Teixeira-Dias, F. (2022), 'Hybrid shielding for hypervelocity impact of orbital debris on unmanned spacecraft', *Appl. Sci.* **12**(14), 7071.

Giannaros, E., Kotzakolios, A., Kostopoulos, V. and Campoli, G. (2019), 'Hypervelocity impact response of CFRP laminates using smoothed particle hydrodynamics method: Implementation and validation', *Int. J. Impact Eng.* **123**, 56–69.

Hayhurst, C. and Clegg, R. (1997), 'Cylindrically symmetric SPH simulations of hypervelocity impacts on thin plates', *Int. J. Impact Eng.* **20**, 337–348.

He, Q., Chen, X. and Chen, J. (2020), 'Finite element-smoothed particle hydrodynamics adaptive method in simulating debris cloud', *Acta Astronaut.* **175**, 99–1.

Johnson, G. (1994), 'Linking of lagrangian particle methods to standard finite element methods for high velocity impact computations', *Nuclear Engineering and Design* **150**(2), 265–274.

Kim, Y., Yoo, J. and Lee, M. (2012), 'Optimal design of spaced plates under hypervelocity impact', *J. Mech. Sci.* **26**(5), 1567–1575.

Livermore Software Technology Corporation (LSTC) (2012), *LS-DYNA Manual, volume I, Keywords user's manual I.*

Nor, M. M., Ho, C., Ma'at, N. and Kamarulzaman, M. (2020), 'Modelling shock waves in composite materials using generalised orthotropic pressure', *Contin. Mech. Thermodyn.* **32**, 1217–1229.

Qu, K., Wu, C., Liu, J., Yao, Y., Deng, Y. and Yi, C. (2020), 'Ballistic performance of multi-layered aluminium and UHMWPE fibre laminate targets subjected to hypervelocity impact by tungsten alloy ball', *Compos. Struct.* **253**, 112785.

Rabiee, A. and Ghasemnejad, H. (2022), 'Finite element modelling approach for progressive crushing of composite tubular absorbers in LS-DYNA: Review and findings', *J. Compos. Sci.* **6**(1).

Raza, H., Garcia, O., Carpenter, K., Pärnänen, T., Jokinen, J., Kanerva, M. and Bayandor, J. (2021), Review of predictive methods for capturing onset of damage and initial delamination in carbon fibre reinforced polymer laminates subject to impact, *in* 'Proc of the 32nd Congress of the International Council of the Aeronautical Sciences (ICAS)', pp. 5–6.

Riedel, W., Nahme, H., White, D. and Clegg, R. (2006), 'Hypervelocity impact damage prediction in composites: Part II — Experimental investigations and simulations', *Int. J. Impact Eng.* **33**(1–12), 670–680.

Ryan, S., Sushma, N., Le, H., Kumar, A., Rana, S., Kandanaarachchi, S. and Venkatesh, S. (2022), The application of machine learning in micrometeoroid and orbital debris impact, *in* 'Proc. of 2022 Hypervelocity Impact Symposium HVIS2022', Alexandria, VA, USA, pp. 1–14.

Salvado, F., Teixeira-Dias, F., Walley, S., Lea, L. and Cardoso, J. (2017), 'A review of the strain rate dependency of the dynamic viscoplastic response of FCC metals', *Prog. Mater. Sci.* **88**, 186–231.

Signetti, S. and Heine, A. (2022), 'Transition regime between high-velocity and hypervelocity impact in metals – A review of the relevant phenomena for material modeling in ballistic impact studies', *Int. J. Impact Eng.* **167**, 104213.

Sinmazçelik, T., Avcu, E., Bora, M. and Çoban, O. (2011), 'A review: Fibre metal laminates, background, bonding types and applied test methods', *Mater. Des.* **32**(7), 3671–3685.

Slimane, S., Slimane, A., Guelailia, A., Boudjemai, A., Kebdani, S., Smahat, A. and Mouloud, D. (2021), 'Hypervelocity impact on honeycomb structure reinforced with bi-layer ceramic/aluminum facesheets used for spacecraft shielding', *Mech. Adv. Mater. Struct.* pp. 1–19.

Soltani, P., Keikhosravy, M., Oskouei, R. and Soutis, C. (2011), 'Studying the tensile behaviour of glare laminates: A finite element modelling approach', *Mater. Des.* **18**, 271–282.

Tepeduzu, B. and Karakuzu, R. (2019), 'Ballistic performance of ceramic/composite structures', *Ceram. Int.* **45**(2), 1651–1660.

Venkatesan, J., Iqbal, M., Gupta, N., Bratov, V., Kazarinov, N. and Morozov, F. (2017), ‘Ballistic characteristics of bi-layered armour with various aluminium backing against ogive nose projectile’, *Procedia Struct.* **6**, 40–47.

Wan, H., Bai, S., Li, S., Mo, J., Zhao, S. and Song, Z. (2013), ‘Shielding performances of the designed hybrid laminates impacted by hypervelocity flyer’, *Mater. Des.* **52**, 422–428.

Wang, X. and Shi, J. (2013), ‘Validation of Johnson-Cook plasticity and damage model using impact experiment’, *Int. J. Impact Eng.* **60**, 67–75.

Whipple, F. (1947), ‘Meteoroid and space travel’, *Astron. J.* **1161**, 132.

White, D., Taylor, E. and Clegg, R. (2003), ‘Numerical simulation and experimental characterisation of direct hypervelocity impact on a spacecraft hybrid carbon fibre/kevlar composite structure’, *Int. J. Impact Eng.* **29**, 779–790.

Wicklein, M., Ryan, S., White, D. and Clegg, R. (2008), ‘Hypervelocity impact on CFRP: Testing, material modelling, and numerical simulation’, *Int. J. Impact Eng.* **35**(12), 1861–1869.

Yong, M., Falzon, B. and Iannucci, L. (2008), ‘On the application of genetic algorithms for optimising composites against impact loading’, *Int. J. Impact Eng.* **35**(11), 1293–1302.

Zhang, A., Zhang, D., Qu, M. and Yu, K. (2015), Numerical simulation on the impact damage of CFRP laminates with different porosities, *in* ‘Proc. of the 10th International Symposium on Measurement Technology and Intelligent Instruments’, pp. 27–30.

Zhang, Y., An, F., Liao, S., Wu, C., Liu, J. and Li, Y. (2022), ‘Study on numerical simulation methods for hypervelocity impact on large-scale complex spacecraft structures’, *Aerospace* **9**(12).

Zhao, Y., Sun, Q., Feng, J., Li, R. and Sun, Y. (2028), ‘Internal-structure-model based simulation research of aramid honeycomb sandwich panel subjected to intense impulse loading’, *Eng. Fract. Mech.* **204**, 1–14.

Zhong, Y. and Joshi, S. (2015), ‘Response of hygrothermally aged glare 4A laminates under static and cyclic loadings’, *Mater. Des.* **87**, 138–148.

Zukas, J. A., Nicholas, T., Swift, H. F., Greszczuk, L. B. and Curran, D. R. (1992), *Impact Dynamics*, Krieger, Malabar, Florida.